Available online at www.sciencedirect.com
ScienceDirect
Acta Materialia 56 (2008) 2955–2965
Acta MATERIALIA
www.elsevier.com/locate/actamat

Fatigue damage initiation and growth from artificial defects in Zr-based metallic glass

B.C. Menzel, R.H. Dauskardt *

Department of Materials Science and Engineering, Stanford University, Stanford, CA 94305-2205, USA

Received 6 December 2007; received in revised form 20 February 2008; accepted 20 February 2008
Available online 24 March 2008

Abstract

An array of well-defined and micrometer-sized circular and line defects were produced on the surface of Zr-based bulk metallic glass bend specimens using a focused ion beam (FIB) in order to study the effect of the defect size, orientation and shape on fatigue damage initiation and growth. Damage evolution was recorded using a surface-replicating technique. Damage was observed to initiate and grow as shear bands or mixed-mode cracks before reaching a characteristic length when they abruptly changed growth direction and propagated orthogonal to the maximum stress axes. Additionally, specimens with circular defect pairs were fabricated so that defect interaction under fatigue loading could be observed. Analysis of the stress state around the defect pairs indicated that damage initiation occurred in regions of highest equivalent (von Mises) stress. Stress-life measurements for bending specimens with FIB surface defects were found to be similar to those for bending specimens without defects at the same applied stress amplitude.

Keywords: Metallic glasses; High cycle fatigue; Fracture; Shear bands; Damage initiation

1. Introduction

Despite their very high monotonic flow strengths, Zr-based bulk metallic glasses (BMGs) have been reported to have surprisingly short fatigue lifetimes and low endurance limits, raising concerns for the structural reliability of these materials [1,2]. Given the very high yield strengths of metallic glasses and their resistance to the initiation of flow under monotonic loading, the observation of low endurance limits and short fatigue lifetimes is surprising. Previous fatigue studies have demonstrated that surface flaws control the stress-life behavior of Zr-based BMG fatigue specimens [2]. Despite the relatively low surface roughness of the specimens (RMS = 0.1 μm), damage was observed to initiate rapidly from the surface asperities and second-phase inclusions. The propagation of damage accounted for almost the entire fatigue lifetime. In the present study a focused ion beam (FIB) was used to fabricate an array of well-defined and micrometer-sized defects on the surface of $Zr_{41.25}Ti_{13.75}Ni_{10}Cu_{12.5}Be_{22.5}$ four-point bending specimens to better understand the influence of surface defects on the early stages of fatigue damage formation and evolution.

The early stages of fatigue damage initiation and growth are often difficult to observe in a specimen with large surface area. Introducing defects at known locations makes tracking damage evolution easier. A linear array of isolated circular and line defects was made to study the effect of defect size, shape and orientation on fatigue damage initiation and growth. A second series of experiments were performed using an array of circular defect pairs to explore the effect of defect interaction. A surface-replicating technique was used to accurately monitor damage evolution throughout the fatigue stress-life test.

Surprisingly, the measured fatigue lifetimes were found to be unaffected by the presence of the FIB defects and measured lifetimes were consistent with those previously reported in four-point bending [1,2]. Damage growth was observed to occur rapidly and to account for almost the

* Corresponding author.
E-mail address: dauskardt@stanford.edu (R.H. Dauskardt).

1359-6454/$34.00 © 2008 Acta Materialia Inc. Published by Elsevier Ltd. All rights reserved.
doi:10.1016/j.actamat.2008.02.029

entire measured stress-life. Damage grew from the FIB defects initially as shear bands or mixed-mode cracks before reaching a critical length and abruptly changing orientations and continuing to grow as a mode I crack until failure. In addition to the damage which initiated at the FIB defects, surface damage also initiated and grew at multiple locations on the surface from the intrinsic surface roughness and naturally occurring inclusions of the specimen. Such damage was found to be as likely to cause failure as damage initiated from the FIB defects. Consistent with earlier observations, fatigue life was observed to be dominated by the damage growth rather than by initiation.

2. Materials and methods

Rectangular specimens 3 mm × 3 mm in cross-section and 40 mm long were machined from a $Zr_{41.25}Ti_{13.75}Ni_{10}Cu_{12.5}Be_{22.5}$ (at.%) fully amorphous bulk metallic plate. Selected mechanical properties are listed in Table 1 [1,3–11]. The specimens were cut from the as-cast plate using electrical discharge machining (EDM) and were mechanically ground and polished on all faces to a final RMS surface roughness of 0.1 μm. The corners of the beam were slightly rounded to reduce stress concentration along the edge of the specimen. The mechanical polishing removed any surface layers containing residual stresses.

The FIB was used to mill two separate defect patterns on the tensile surface of the specimen (along the inner span of the beam) as depicted in Fig. 1a and b. The first defect pattern (Fig. 1a) consisted of a linear array of simple circular and line defects. All defects were milled to depths equal to one-half of their characteristic length: radii R, for circular defects and surface half-length, c, for line defects. Circular defects were milled with R of 2.5 and 10 μm. The radii of the circular defects were essentially constant with depth. The linear defects were fabricated at angles of 45° and 90° to the maximum tensile stress direction and were milled with

Table 1
Selected mechanical properties of fully amorphous $Zr_{41.25}Ti_{13.75}Ni_{10}Cu_{12.5}Be_{22.5}$ (at.%) BMG [1,3–12]

Property	Value
Young's modulus, E	95 GPa
Shear modulus, G	35 GPa
Poisson's ratio, ν	0.35
Ultimate tensile strength, σ_{UTS}	1.9 GPa
Coefficient of internal friction, μ	0.038
Vickers hardness	5.4 GPa
Fracture toughness, K_{IC}	~16–55 MPa $m^{1/2}$
Endurance limit, σ_e[a,b]	~170–200 MPa
Fatigue crack growth threshold, ΔK_{TH}[a]	~1.5–2 MPa $m^{1/2}$
Fatigue crack growth parameter, m[a]	1.7
Fatigue crack growth parameter, C[a]	2.4×10^{-10}
Glass transition temperature, T_g	625 K
Average relaxation time, τ[c]	450 s
Density, ρ	5.9 g cm^{-3}

[a] $R = 0.1$.
[b] Measured in bending.
[c] Measured at 416 K.

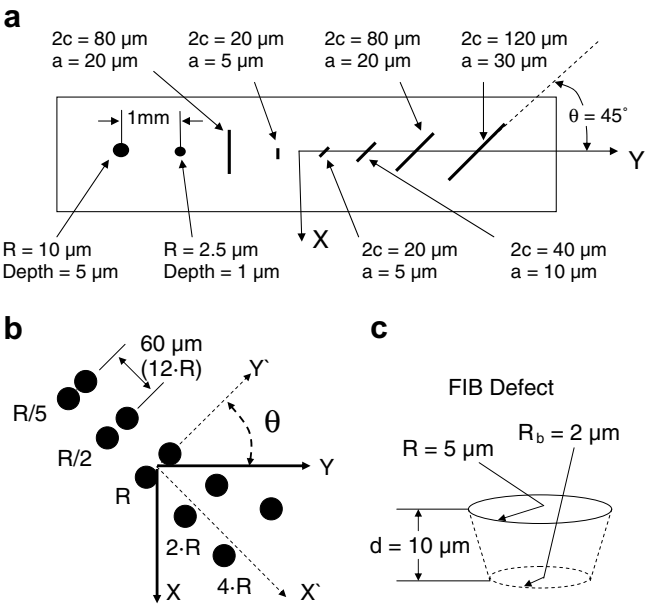

Fig. 1. FIB defect patterns employed showing (a) a linear array of circular and line defects (pattern 1) where c is the surface half-length, a is the defect depth, and R the defect radius; (b) an array of circular defect pairs (pattern 2) at angle θ to the loading axis with radius R on the specimen surface and selected separations; and (c) the three-dimensional conical geometry of the circular defects shown in (b).

surface lengths ($2c$) ranging from 20 to 120 μm. Scanning electron microscopy (SEM) images of a circular and a line defect are shown in Fig. 2a and b. The aspect ratio of the line defects was chosen to roughly approximate the aspect ratio observed for the growth of surface defects reported previously in this material [1,2]. Each defect was centered along the middle of the beam's width and separated from its nearest defect neighbor by a distance of ~1 mm to prevent any defect–defect or defect–edge interaction.

The second defect pattern (Fig. 1b) consisted of five separate circular defect pairs at varying distances from each other and at varying angles to the maximum tensile stress direction. The radius of each defect was held constant at $R = 5$ μm and the distance between the defects were increased as a function of R from $R/5$ to $4R$. Each defect pair was separated from its nearest neighbor by a distance of ~12 R to prevent the stress fields from one defect pair overlapping with another. The pattern was milled along the inner span of the beam (with the pattern centered on the middle of specimens surface) at angles of $\theta = 15°, 30°, 40°, 45°, 60°$, and 90° to the maximum tensile stress direction. An SEM image of the pattern milled at $\theta = 60°$ is shown in Fig. 2c. Due to the limitations of the milling process and the aspect ratios chosen for the circular defects, the defects were not perfect cylinders; they were found to have a radius of ~2 μm at a depth of 10 μm, leading to a cone-like shape as depicted in Fig. 1c.

It is possible that the local structure of the glass at the edges of the defects could have been altered during the ion milling process. All defects were milled with an ion

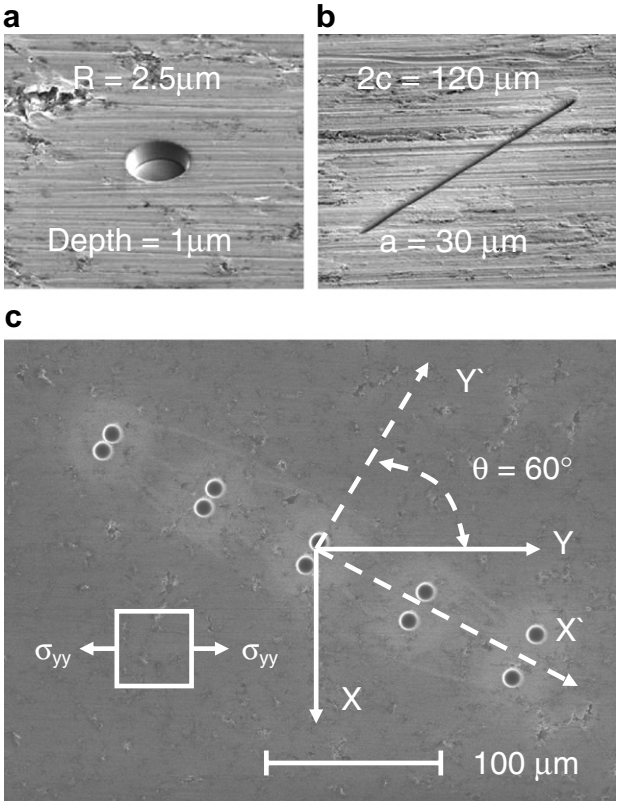

Fig. 2. SEM images of the FIB defects showing (a) a circular defect from the linear defect array with $R = 2.5$ μm and depth = 1 μm; (b) a line defect with $2c = 120$ μm and $a = 30$ μm; and (c) the complete pattern of pair defects milled at $\theta = 60°$.

current of 20,000 ρA at 30 keV. Changes could have occurred via local heating and quenching of the glass during million or through structural changes due to the physical impact of the milling ions. FIB milling parameters were selected such that it would produce a minimal altered region of the glass. High-resolution SEM imaging was conducted at 5 keV and revealed no obvious changes to the glass structure, and no further characterization was performed to detect any local changes in the glass structure around the FIB defects.

All specimens were loaded using a fully articulating four-point bend fixture with an outer, S_o, and inner, S_i, span of 30 and 10 mm, respectively, in a servohydraulic mechanical test system. Testing was conducted under load control using a sinusoidal waveform and a load ratio of $R_L = 0.1$. A nominal frequency of 5 Hz was employed. The number of loading cycles to cause failure, N_f, was determined. A single cycle was defined as a complete stress reversal. Testing was conducted in ~50% relative humidity laboratory air at 25 °C. The test frequencies employed represent loading time scales that are well below the relaxation timescale at the test temperature to avoid gross viscoelastic deformation of the material [9]. The testing conditions employed resulted in stress-life data consistent with those previously reported [1,2].

The constant bending moment along the inner span of the four-point beam specimen produces a uniform maximum normal tensile and compressive stress on the top and bottom surfaces of the specimen, respectively. The damage observed occurred on the tensile surface of the specimen. The normal tensile stress obtained from simple beam mechanics is

$$\sigma = \frac{3P(S_o - S_i)}{2bh^2}, \tag{1}$$

where P is the applied load, h is the specimen height, and b is the specimen thickness. Beams were tested with σ in the range of 550–1267 MPa and tests were terminated if failure did not occur in 2×10^7 cycles. Stress-life data is presented in terms of stress amplitude ($\sigma_a = (\sigma_{max} - \sigma_{min})/2$) normalized by the ultimate tensile strength of the material (σ_{UTS}), where σ_{max} and σ_{min} correspond to the maximum and minimum values of the applied loading cycle, respectively. The flow behavior of this material is elastic-perfectly plastic, resulting in an ultimate tensile strength equal to the yield strength, σ_{ys}.

A cellulose acetate replicating tape was used to record the initiation and growth of surface damage during the fatigue test. Acetate tape was softened with acetone and held against the tensile surface of the specimen until the acetone evaporated and the tape hardened. All replicas where produced, while the specimens were held at the median load of the fatigue loading cycle. Features on the specimens surfaces were reproduced on the acetate negatives with a nominal resolution of ~10 nm. To quantify the initial state of the specimen surface, replicas were created at the tests' median load prior to cycling. Once cycling began, the tests were halted periodically at the median load in order to fabricate additional replicas. The surface was rinsed with acetone before and after each replica was produced to remove any residual acetate. After testing, the final replica was examined first so that the damage that caused failure could be identified and traced back to the initial replica made before cycling.

The replicas fracture and tensile surfaces of the specimens were examined using SEM to characterize the onset and evolution of fatigue damage. Prior to SEM examination, the replicas were coated with a thin layer of gold. Comparison of the final replica and the corresponding tensile surfaces were used to verify the accuracy of the replicas. Damage was apparent in the form of shear bands or surface cracks that could be easily identified on the replicas. The fracture surfaces of the specimens were carefully examined to determine possible initiation and growth mechanisms, crack geometry, critical crack length, and other salient features of the initiation sites. Atomic force microscopy (AFM) was performed to quantify the surface roughness of the beams.

3. Results

The numbers of cycles to failure, N_f, measured as a function of the normalized applied stress amplitude, σ_a/σ_{UTS},

are presented in Fig. 3. Specimens with a linear array of defects (Fig. 1a) were tested at $\sigma_a/\sigma_{UTS} = 0.13$, while specimens with circular defect pairs (Fig. 1b) were tested at $\sigma_a/\sigma_{UTS} = 0.3$. For all specimens, failure occurred within the inner span of the beam. As is clearly apparent in Fig. 3, the stress-life results were consistent with published results for nominally defect-free specimens of the same glass composition [1,2]. Also included in the figure is the stress-life curve for a high-strength steel with an ultimate tensile strength of 2.3 GPa [12], similar to that of the glass. The endurance limit, operationally defined as the maximum stress amplitude that the material could be subjected to for 2×10^7 cycles without failure, was $\sim\sigma_a/\sigma_{UTS} = 0.05$. The reported endurance limit is less than 10% of the ultimate tensile strength and in stark contrast to typical high-strength polycrystalline metals which exhibit endurance limits of $\sim 0.5\ \sigma_{UTS}$.

Examination of surface replicas taken from tests conducted using the linear defect pattern (Fig. 1a) showed that when the defect length was below a critical length for both circular and line defects, damage initiated as shear bands or mixed-mode cracks after only a few stress cycles and propagated at $\sim 49^o$ to the maximum normal stress axis, as seen for a line defect in Fig. 4. Damage abruptly changed orientation after reaching a critical length, and grew as mode I cracks until failure. This critical surface half-length was measured previously to be 40–70 μm for semi-elliptical surface cracks tested at $\sigma_a/\sigma_{UTS} = 0.13$. For linear FIB defects longer than the critical length, damage grew immediately under mode I conditions and no mixed-mode/shear band growth was observed. Additionally, defects oriented perpendicular to the tensile stress direction with lengths greater

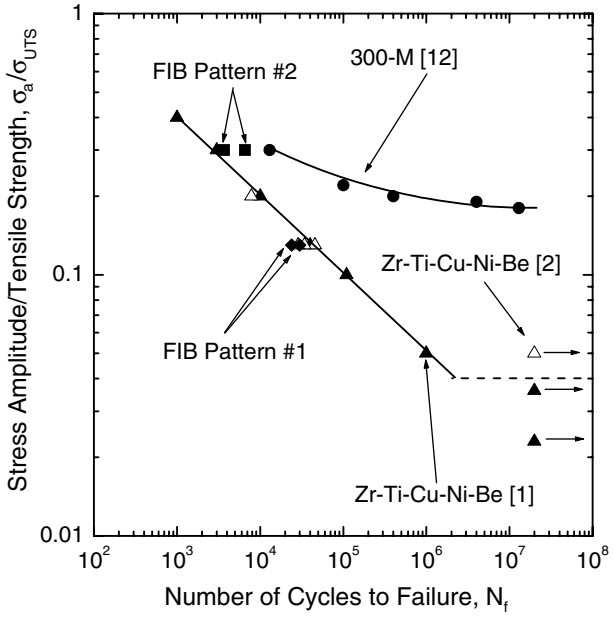

Fig. 3. Measured stress-life fatigue data for bend specimens containing the defect patterns compared to data from bending tests of the same BMG material [1,2] and a high-strength steel alloy [12].

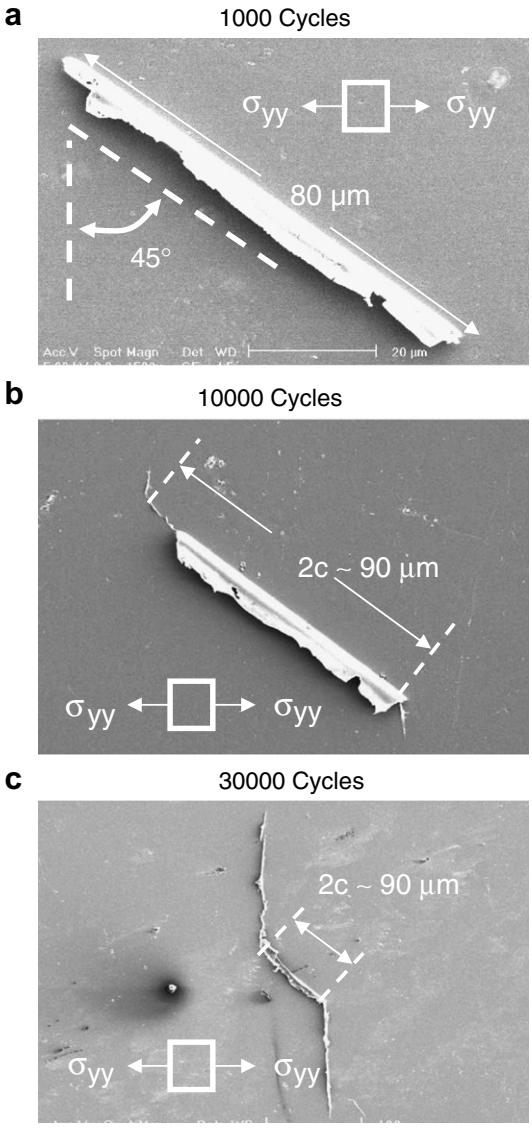

Fig. 4. SEM images of surface replica from a linear FIB defect showing (a) the defect before damage growth, (b) shortly after fatigue damage has changed growth directions, and (c) continued fatigue damage growth perpendicular to the applied tensile stress.

than the critical defect size did not exhibit any mixed-mode growth. The number of cycles to initiate and grow damage to the critical length was similar to that observed in tests without FIB defects. Note that the compressive surfaces of the beams exhibited no observable fatigue damage.

Schematic illustrations representing the different stages of damage growth for surface cracks are shown in Fig. 5. Initially damage grows under mixed-mode conditions and was modeled as a semi-elliptical surface crack as shown in Fig. 5a. The tensile axis is aligned with the Y direction in the XYZ coordinate system and the $X'Y'Z'$ coordinate system is aligned with the cracks' natural coordinate system. The length c represents the damage half-length along the sample surface, while the length a represents the length of the damage into the specimen. The angle θ represents the rotation of the crack with respect to the tensile direction,

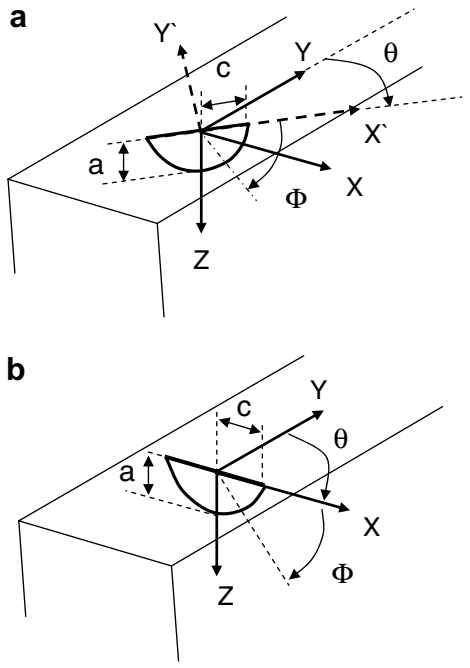

Fig. 5. Idealized crack geometries showing (a) the semi-elliptical surface crack under mixed-mode loading, and (b) semi-elliptical surface crack under mode I loading.

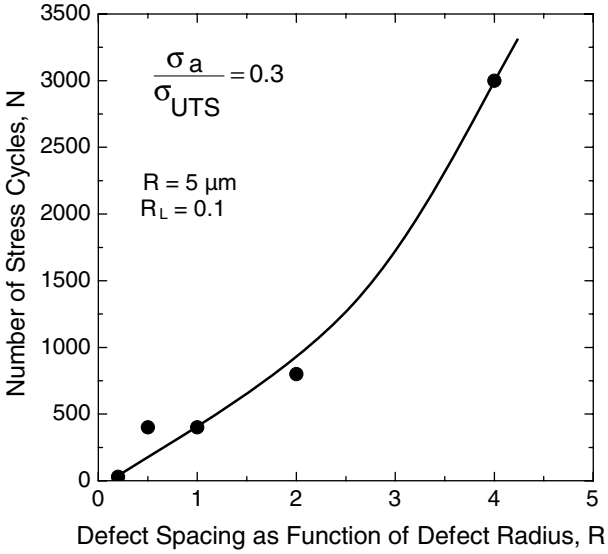

Fig. 6. The number of cycles, N, required for the first observable fatigue damage as a function of defect spacing, R, for $\theta = 0°$. All results were taken from a single specimen.

while angle Φ is used to determine the position of a point along the crack front. After damage reached a characteristic length, it kinks in the mode I direction. When the kinks have grown longer than the parent crack, damage can be again modeled as a semi-elliptical surface crack as shown in Fig. 6b. Here, $\theta = 0°$ and the critical stress intensity factor, K_{IC}, at final fracture was calculated to be $\sim$15 MPa m$^{1/2}$ using published stress intensity solutions for semi-elliptical surface cracks [13,14]. This value is consistent with plane strain fracture toughness values previously reported [10,11].

A strong dependency between damage initiation and defect spacing was observed during the defect pair study. As the defect spacing became smaller (Fig. 1b), the interaction of the defect stress fields increases, leading to more rapid damage initiation as shown in Fig. 6 for defects oriented perpendicular to the tensile stress direction. This trend was similarly observed for all orientations of defects with respect to the applied tensile stress.

A SEM image of a circular defect pair with spacing of $2R$ and an angle of 45° ($\sigma_a/\sigma_{UTS} = 0.3$) taken at the end of a test (6572 cycles) is shown in Fig. 7a. A replica taken earlier during the test (3000 cycles) for the same pair is shown in Fig. 7b. Additionally, a replica taken of defect pairs with spacing of $R/2$ ($\theta = 90°$) and $4R$ ($\theta = 40°$) at 3000 cycles from a different test are included in Fig. 7c and d, respectively. A schematic showing the pertinent defect pair geometry is given in Fig. 8, where the applied tensile stress direction is parallel to the Y (or Y') axis. The angle θ again represents the orientation of the defect pair with respect to the applied tensile stress direction. The points A and A′ are located between the centers of the defects and along the edge of their respective defect. The points B and B′ are located along the outside edges of the defect pair. The shaded region on the face the defect in Fig. 8 represents an area, where the von Mises or equivalent stress is above the yield strength of the material (for $\sigma_a/\sigma_{UTS} = 0.3$). The equivalent stress is given by

$$\sigma_e = \left[\frac{(\sigma_1 - \sigma_2)^2 + (\sigma_2 - \sigma_3)^2 + (\sigma_1 - \sigma_3)^2}{2}\right]^{1/2}. \quad (2)$$

where σ_1, σ_2, and σ_3 correspond to the principal stresses. When $\sigma_e \geqslant \sigma_{ys}$, yielding is predicted to occur. This region is bounded by the angles θ_1 and θ_2, which are determined by the exact defect pair orientation. Damage was observed to always initiate in this region, typically along the edge of the defect and the surface of the sample at or near points A, A′, B or B′ for $\theta = 90°$. For $\theta = 15$–$60°$, damage was observed to initiate over the range from $\theta_1 = 62°$ to $\theta_2 = 118°$. It was observed that initiation was as likely to occur between the defects (A or A′ side) as it was outside of the defects (B or B′ side).

Following initiation, damage generally propagated completely across the defect where it initiated, for example, from point A to point B before propagating along the surface of the specimen. Once damage had completely propagated across the defect, continued growth along the surface was controlled by defect spacing and orientation. For pairs oriented at $\theta = 90°$, surface damage growth was perpendicular to the applied tensile stress direction (Fig. 7c). For $\theta = 15$–$60°$, growth along the surface was strongly dependent on the spacing of the defects. For closely spaced defects, $R/5 - 2R$ damage was typically observed to grow between the defects as seen in Fig. 7a. However, for large defect spacing, 4R, damage was again observed to grow perpendicular to the applied tensile stress as seen in Fig. 7d.

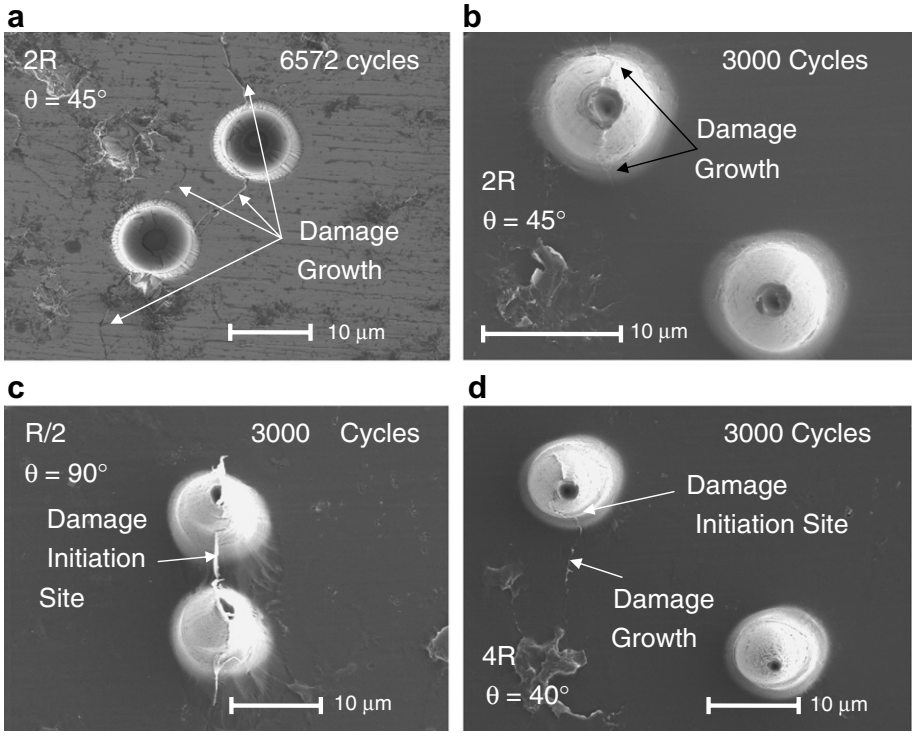

Fig. 7. SEM images of surface and surface replica showing (a) fatigue damage on the specimen tensile surface for defects oriented at $\theta = 45°$ and separated by $2R$; (b) a replica showing early damage growth for the defect pair shown in (a); (c) a replica of damage growth for $\theta = 90°$ and spacing of $R/2$; and (d) a replica of surface damage for a defect pair oriented at $\theta = 40°$ and separated by $4R$.

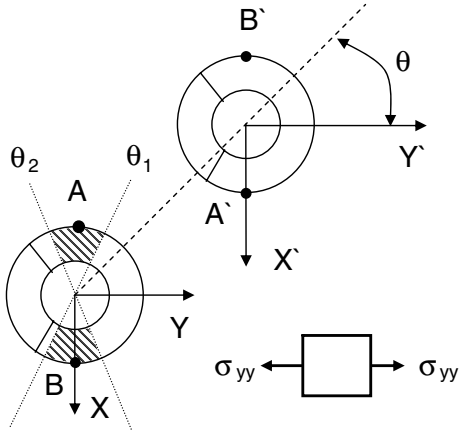

Fig. 8. Schematic illustration of a circular defect pair oriented at an angle θ to the applied tensile stress direction. The shaded areas represent regions of elevated equivalent stress inside the defect where damage was observed to initiate.

Damage did not initiate and grow from every FIB defect during fatigue testing. Initiation and growth was also observed at surface locations other than the FIB defects. Flaws existed on the surface in the form of fine scratches, trenches and pits, most likely introduced during the polishing process but did not have features significantly higher than the surface RMS roughness of 0.1 μm. The roughness-induced damage initiation was found to be as likely to cause failure as the FIB defects. For specimens with patterns of FIB defect pairs, damage was more often observed to grow from defect pairs at angles of $\theta = 40°, 45°, 60°$ and 90° and rarely observed for defects at angles of $\theta = 15°$ and 30°. It was typically observed that the greater the aspect ratio of the line defect, or the closer the spacing of a defect pair, the more likely it was that these defects would initiate fatigue damage and subsequent growth.

Fractographic evidence revealed that once the damage had reached a critical length it abruptly changed direction and began to propagate perpendicular to the applied tensile stress axis. Growth occurred by stable fatigue crack growth and the crack adopted a semi-elliptical geometry with an aspect ratio of $c \approx 1.5a$, as previously observed [2]. Stable crack growth occurred via an apparent fatigue-like striation mechanism. "Ridge"-like markings similar to those reported in previous investigations were observed running parallel to the crack front on the facture surface [1]. A veined fracture surface morphology was apparent when unstable fracture occurred at the end of the test. The demarcation between the stable and unstable crack growth regions was readily apparent on all fracture surfaces. This allowed the critical crack length to be determined directly from the fracture surfaces.

4. Discussion

It was shown for nominally defect-free Zr-based BMG specimens under bending that damage evolution occurred after very few fatigue loading cycles [2]. The measured stress-life curve was dominated by the number of cycles

needed to propagate damage to a critical size, unlike high-strength single or polycrystalline metallic materials where damage initiation typically accounts for the majority of high-cycle fatigue life. For the present BMG, since the majority of the fatigue life results from damage propagation, the presence of the micron-sized FIB defects has little affect on life (Fig. 3). Surface replicas of specimens clearly indicated that damage initiation associated with the FIB defects occurs very rapidly (Figs. 4 and 7), but since life is growth dominated, this has no discernible affect on fatigue life. We note that a recent fatigue study reported significantly longer initiation times for a similar Zr-based metallic glass and ascribed the behavior to the absence of surface residual stresses [15]. However, as noted above, we did not observe such behavior in our fatigue specimens, which were machined to remove any residual surface stresses.

It is now well documented that the onset of flow in BMG materials (including Zr-based alloys) follows a Mohr–Coulomb type relationship [16–20]:

$$T_c + K_o - \mu\sigma_n, \tag{3}$$

where T_c represents the resolved shear stress on the slip plane where flow occurs, K_o is the yield strength of the material in pure shear, μ is the coefficient of internal friction, and σ_n is the normal stress acting on the slip plane. For uniaxial monotonic compression and tension, yielding occurs by strain localization in the form of slip along shear bands [16–20]. Failure occurs by unstable fracture along the weakened material of the shear band. Due to the normal stress flow dependency, slip does not occur on the plane of maximum resolved shear stress. Under compression, the failure surface is less than 45° and in uniaxial tension tests the failure surfaces is typically oriented at angles between 50° and 59° to the loading axis depending on the value of μ [16–19]. For the present glass $\mu \sim 0.038$, which is small compared to other dilatant-sensitive materials such as soils and rock which might exhibit coefficients of internal friction in the range of 0.3–0.6 [21].

Damage initially propagated at ~49° to the tensile axis from the linear array of surface defects with initial size below the critical length (Fig. 4). This angle is in agreement with what has been observed experimentally under monotonic loading and for surface fatigue cracks [2]. After reaching a critical length, the damage abruptly changed growth direction and continued to propagate perpendicular to the tensile axis (Fig. 4). It is likely that damage first propagates as a shear band before mode I crack growth occurs. In the absence of microstructure and crystalline slip systems, the angle of the initial flow appears to be determined by the Mohr–Coulomb flow criteria. In addition, examination of the fracture surfaces revealed that the mixed-mode region was featureless and the presence of striations was not observed, another indication that damage propagated via a shear band rather than a mixed-mode crack. After changing orientation, the fracture surface exhibited the "ridge"-like features characteristic of a mode I fatigue crack [2]. However, it should be noted that the exact nature of the initial damage evolution in the form of a shear band or mixed-mode crack could not be determined unambiguously and remains uncertain.

The Rice–Rudnicki model for the localization of deformation in pressure-sensitive materials was explored to further clarify, whether or not the initial mixed-mode region could correspond to a shear band [22]. This model helps to predict whether or not strain localization will occur in a material with a normal stress flow dependency. The strain localization predictions considered here are based on an isotropic hardening constitutive model. The model predicts both the critical hardening modulus, h_{cr}, that the material must possess to prevent flow localization and the orientation of the strain localization plane. The hardening modulus is related to the tangent modulus:

$$h_{tan} = \frac{h}{1 + \frac{h}{G}}, \tag{4}$$

where G is the shear modulus of the material. The relevant material properties of the glass used in this investigation were $\mu = 0.038$, $G = 35$ GPa and $v = 0.35$. The dilatancy factor, β, for the material is unknown and a reasonable value was taken to be equal to μ, consistent with the normality rule of plasticity. Dilation studies on a Pb–Cu–Si glass system yielded $\beta = 0.018$, again suggesting that dilatancy effects for metallic glasses are small [23]. Using an axially symmetric applied tensile load ($\sigma_I > \sigma_{II} = \sigma_{III} = 0$) and the given material properties, h_{cr}/G was calculated to be -0.2, suggesting that the glass must exhibit strain softening for localization to occur. Rapid strain softening in the glass following a peak elastic stress is consistent with the theoretical flow models proposed for metallic glasses [24–26]. Experimental results from numerous compression tests suggest that metallic glasses exhibit macroscopically elastic-perfectly plastic stress–strain behavior [16,20,27,28]. However, detailed recent studies of the plastic portion of the stress–strain curve show sharp serrations in the plastic portion of the loading curve [20,27]. The rapid decrease in load following the formation of these sharp serrations may be the result of rapid softening of the glass along the active shear band in the specimen. The model was also used to predict θ_o, which is the angle that defines the plane of localization; in this case it is equal to the angle between the shear plane and the applied tensile stress direction. A value of $\theta_o = 49°$ was found, in exact agreement with the angle observed for the formation of surface shear bands under fatigue loading and similar to the angle observed under monotonic loading for this glass. The Rice–Rudnicki model therefore seems to suggest that the initial deformation in the metallic glass corresponds to the localization of flow along a shear band.

The bending stresses applied to the specimens in this study are well below the tensile strength of the material. Stress concentrations due to the presence of FIB defects or surface roughness on the tensile surface significantly elevate the local stresses, possibly leading to the initiation of

local flow. The sharpness of the line defect is limited to the spot size of the ion beam, which is finite in diameter and circular in shape, leading to a defect that has an initial tip radius, $\rho \sim 1$ μm. The stress concentration factor K_t for a semi-elliptical through-crack under mode I loading is

$$K_t = 2\sqrt{\frac{c}{\rho}}, \tag{5}$$

where c is the crack half-length. Given the high aspect ratio of the linear FIB defects, this yields a stress concentration factor of ~9–18 for defects with an initial length $2c$ of 20–80 μm. The circular defects have a stress concentration factor of 3 that is not affected by the diameter of the defect. At $\sigma_a/\sigma_{UTS} = 0.13$, defects would only need a stress concentration factor of 3–4 to raise the local stress above the yield strength and initiate flow. Damage would therefore be expected to initiate at each FIB defect tested at $\sigma_a/\sigma_{UTS} \geqslant 0.13$. Indeed, damage was observed to initiate for both the circular and line defects at these applied stress levels.

The RMS roughness of the 300-M steel included in Fig. 3 was reported to be 1.6 μm [12], much greater than the 0.1 μm roughness of the metallic glass specimens. One reason why crystalline materials such as 300-M can tolerate such roughness without drastic reductions in their endurance limit may be associated with strain-hardening behavior, which inhibits flow, unlike metallic glasses which do not exhibit significant strain-hardening. Crystalline materials such as steels also exhibit homogeneous plastic flow which would cause blunting of the defect and reduction of the stress concentration effect. In metallic glasses, shear banding from an initial defect is not likely to cause blunting of the stress concentration and may actually lead to an increased stress concentration at the tip of the shear band.

Once surface damage reaches a critical length for a given load (Fig. 4b), it abruptly switches orientation and continues to propagate as a mode I fatigue crack. The numerical solutions for semi-elliptical cracks are available in the literature, allowing the stress intensities along the crack front can be calculated at the maximum load of the fatigue loading cycle for the geometries shown in Fig. 5a and b [13,14]. Such calculations were performed and published previously [2]. These solutions can be used to rationalize the switching mechanism between mixed-mode and mode I growth. From the stress intensity calculations for these configurations, it is apparent that the critical length at which switching occurs corresponds to the mixed-mode crack length, when the K_I component just equals the mode I fatigue crack growth threshold, ΔK_{TH}. For long cracks $\Delta K_{TH} \sim 1.5$–2 MPa $m^{1/2}$ for the present material [3]. A plot of the critical crack length vs. the normalized applied stress is provided in Fig. 9. An SEM image taken from a replica of a linear defect is shown in Fig. 4. For $\sigma_a/\sigma_{ys} = 0.13$ a crack is predicted to switch orientations after reaching a surface half-length $c \sim 42$ μm. Damage initially grows in the mixed-mode direction since the crack-like FIB defect is initially shorter than the critical length. Once damage has grown longer than the critical length, it abruptly switches orientation and continues to grow in a mode I orientation.

For specimens without FIB defects tested at $\sigma_a/\sigma_{ys} = 0.13$, the number of cycles needed to initiate the initial fatigue damage to the critical length was ~10,000 cycles. This represents ~25% of the total fatigue life, which is relatively small compared to the initiation time for most high-strength crystalline metals. For specimens with linear and circular FIB defects tested at $\sigma_a/\sigma_{ys} = 0.13$ the number of cycles need to grow damage to the critical length was between 1000 and 10,000 cycles (Fig. 4), similar to samples without any initial defects. Damage which initiated from the circular defects followed similar trends to the line defects. The local stress concentration was high enough to cause flow and mixed-mode damage growth was observed. When the damage reached the critical length it abruptly switched orientations in the same fashion as the linear defects.

In order to analyze the defect pair interactions the elastic stress fields were calculated using a commercial finite-element package. A well-refined mesh of 10 node tetrahedral elements was employed. Contour plots of the equivalent stress for $\theta = 90°$ $R/2$, $\theta = 45°$ $2R$ and $\theta = 40°$ $4R$ are plotted in Fig. 10; an example of the finite-element mesh is shown as well. For simplicity a state of constant uniaxial stress equal to the maximum bending stress ($\sigma = 1267$ MPa for $\sigma_a/\sigma_{ys} = 0.3$) at the tensile surface of the bend specimen was imposed on the block of material containing the defect pair. In the actual specimen the bending stress decays linearly from the surface of the specimen.

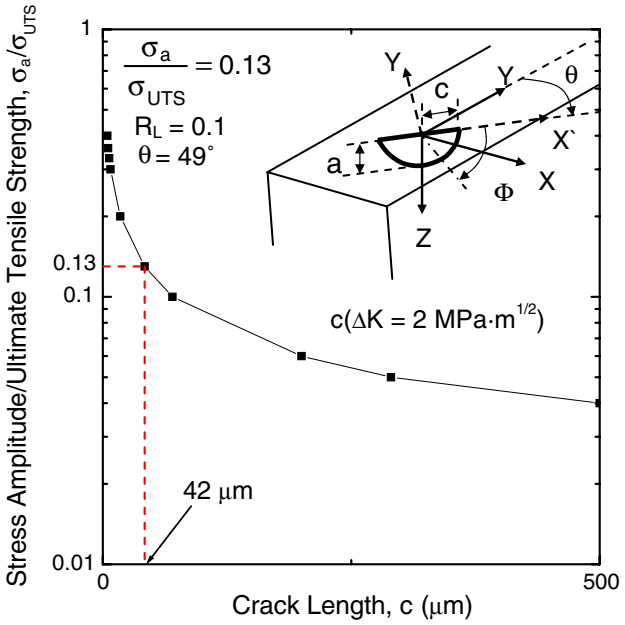

Fig. 9. Calculated critical crack length in terms of the applied stress amplitude for a mixed-mode surface crack to achieve a value of $\Delta K = 2$ MPa $m^{1/2}$ equal to the fatigue crack growth threshold, ΔK_{TH}. Switching of the mixed-mode crack into a mode I crack is predicted at this crack length.

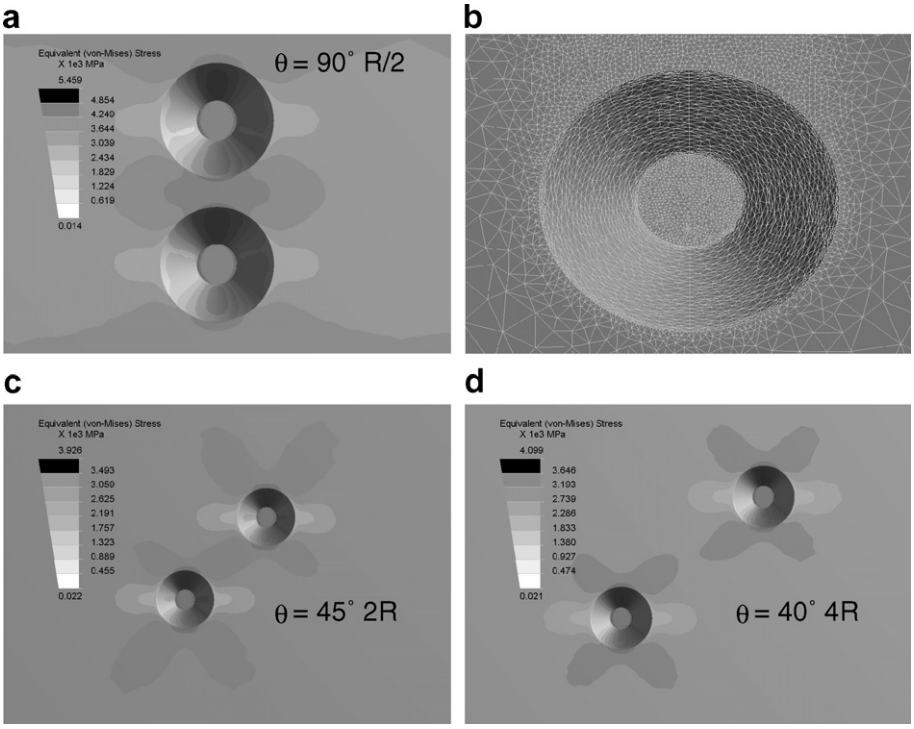

Fig. 10. Finite-element results for circular defect pairs for a load of $\sigma_a/\sigma_{UTS} = 0.3$ and load ratio $R_L = 0.1$, showing (a) the equivalent stress for defect pairs at $\theta = 90°$ and separated by $R/2$; (b) the finite-element mesh for results in (a); and the equivalent stress for defect pairs (c) oriented $\theta = 45°$ with separation $2R$, and (d) oriented $\theta = 40°$ with separation $4R$.

However, since the defects are only 10 μm deep the stress decay in the specimen is less than ~1% and would have little effect on the calculated stress fields. The aspect ratio, orientation and the spacing of the defects was consistent with the actual specimens. The block containing the defect pair was large enough in all cases to avoid any interaction between the edges and the defects.

The calculated equivalent stress distribution closely matches that of the σ_{yy} stress due to the relative magnitude of the σ_{yy} stress compared to the other stress components. The stress distribution within a single defect was not much affected by the orientation of the pair to the applied stress direction as seen in Fig. 10. The highest equivalent stress was located along the bottom corner of the defect at $\theta \sim 0°$ and 180°. No attempt was made to round the bottom corner of the defect in the finite-element simulation. The bottom corners of the actual defects are slightly rounded, which probably alleviates some of the stress concentration observed in the finite-element calculations. An indication of the interacting stress fields was obtained by plotting the highest equivalent stress normalized by the applied stress along the outer edge of the defect on the A and B sides of the defect as a function of spacing R in Fig. 11 for orientations of $\theta = 15°, 30°, 45°, 60°$ and 90°.

When the results of the finite-element calculations (Fig. 10) are compared with the damage initiation sites identified on the surface replica (Fig. 7), it is apparent that damage initiation corresponds to regions of higher equivalent stress. Damage most often initiated at the edge of the defect and the surface of the specimen in the region where the equivalent stress was greater than the flow strength of the glass (shaded region in Fig. 8). Damage was found to initiate as often on the outside side of one of the defect pairs (near B or B′) as between the pair (near A or A′) for larger defect spacings. This is probably associated with the similarity of the stress on the A and B sides of the defect for large defect spacings. The actual variation of the initiation location along the edge of the defect may be due to the stochastic nature of fatigue and local fluctuations in surface properties along the defect, including both material strength and surface roughness.

A strong dependency between damage initiation and defect spacing was observed during the defect pair study. As the defect spacing decreased, the interaction of the defect stress fields increased, leading to higher stresses and lower fatigue cycles needed for damage initiation. The number of cycles for damage initiation is plotted in Fig. 6 as a function of defect spacing for $\theta = 0°$ and $\sigma_a/\sigma_{ys} = 0.3$ and exhibits a rapid decrease as the defect spacing decreases. Little damage initiation was observed for orientations of $\theta = 15°$ and 30°. The defects are oriented in such a way that the compressive field surrounding one defect interacts strongly with the tensile field of the other, leading to a much lower stress concentration than other orientations as shown in Fig. 11.

Some additional general trends were observed, further elucidating the detailed early damage growth processes. Damage first grows completely across the defect (e.g. from

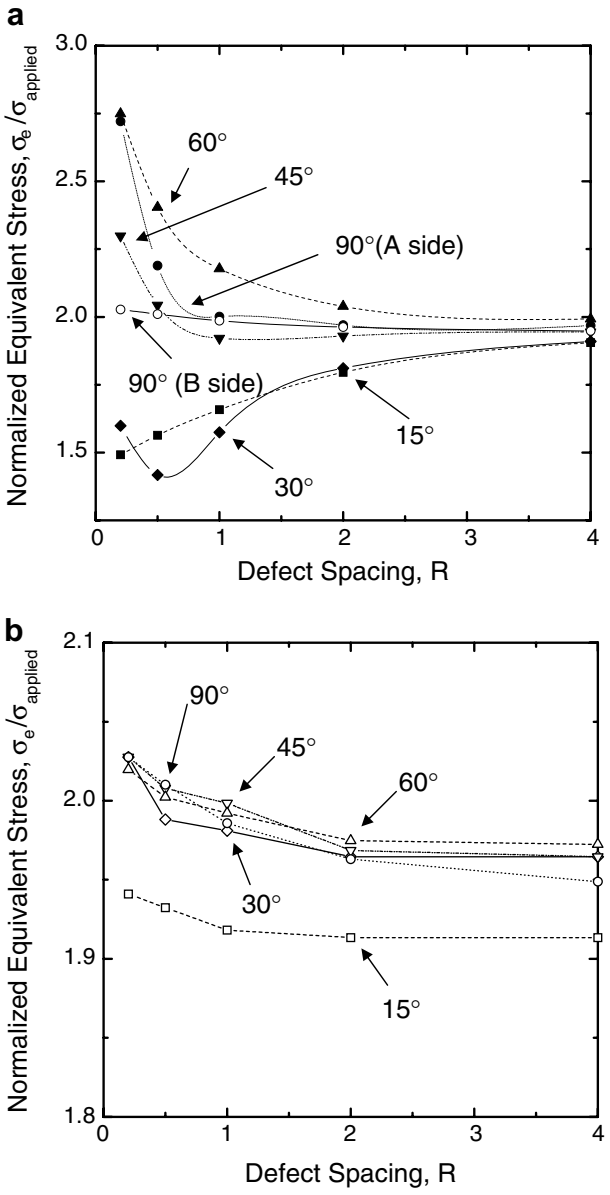

Fig. 11. Maximum normalized equivalent stress as a function of defect spacing and orientation, θ, for $\sigma_a/\sigma_{UTS} = 0.3$ and load ratio $R_L = 0.1$ showing (a) the A side of the defect, and (b) the B side of the defect.

A to B) essentially following the path of highest equivalent stress (compare Figs. 7 and 10) before propagating along the surface of the specimen. The path of damage propagation along the tensile surface of the specimen is then determined by the distribution of equivalent stress around the defects, which is a function of the defect spacing and orientation. On the surface of the specimen the equivalent stress are highest roughly along the path connecting the upper edge of the lower defect and the lower edge of the upper defect (point A to point A′ in Fig. 8). As the defect spacing increases, the concentration of stress along that path decreases, and at the largest spacing ($4R$) there is essentially no path of elevated stress between the defects (Fig. 10d). For large defect spacing, growth is no longer promoted between the defects and damage is observed to grow in essentially a mode I fashion once it transverses from one side of the defect to the other. A semi-elliptical surface crack with $c = 5$ μm, $a = c$ and $\theta = 90°$ under a load of $\sigma_a/\sigma_{ys} = 0.30$ ($R_L = 0.1$) has $\Delta K = 3.3$ MPa m$^{1/2}$ at $\Phi = 0°$. Although damage at this stage is not a semi-elliptical surface crack and the stress concentration of the defect is not considered, this simple analysis suggests that mode I fatigue crack growth should occur without any mixed-mode growth, which is consistent with what is seen on the replica for defect spacing of $4R$ (Fig. 7d). For closer defect spacing, where there is an appreciable elevation of the equivalent stress between the defects, damage is observed to grow along that path between the defects. Once the damage has propagated across and between both defects, mode I growth was always observed.

We have demonstrated that the local stress fields associated with the circular defects can be used to significantly affect the initiation cycles to form fatigue damage. In addition, the separation and orientation of the defects can be used to steer the growth direction of the shear bands. We hope that the work will therefore form the basis for using such artificial defects to study the initiation of shear bands, to further explore the role of fatigue loading parameters, and possibly also to help design composite metallic glass microstructures with optimum distributions of second-phase particles to distribute shear bands and improve mechanical properties.

5. Conclusions

An array of well-defined and micrometer-sized circular and line defects were produced on the surface of Zr-based BMG bend specimens using a FIB to study the effect of the defect size, orientation and shape on fatigue damage initiation and growth. Measured stress-life was not reduced significantly for specimens containing the defects compared to specimens without defects. Rapid damage growth was observed from the defects as well as from other surface locations. Fatigue life was related to the growth rather than initiation of fatigue damage. Damage typically grew initially from the defects under mixed-mode conditions before reaching a critical length where it abruptly changed orientation and continued to grow in a mode I direction until failure. Prediction from the Rice–Rudnicki model as well as examination of the fracture surfaces suggests that the initial mixed-mode growth corresponds to shear band growth. The switching phenomena correspond to a length where the mode I stress intensity component at the tip of the mixed defect reached the fatigue crack growth threshold. Damage initiation sites for the defect pairs were observed to be located in regions of highest equivalent stress.

Acknowledgments

This research was supported by a grant from the Boeing Corporation. The authors thank Drs. T.W. McGann and

J.D. Cotton of the Boeing Corporation for their support of the research.

References

[1] Gilbert CJ, Schroeder V, Ritchie RO. Metall Mater Trans A 1999;30A:1739.
[2] Menzel BC, Dauskardt RH. Acta Mater 2006;54:935.
[3] Flores KM, Johnson WL, Dauskardt RH. Scripta Mater 2003; 49:1181.
[4] Johnson WL, Peker A. In: Otooni MA, editor. Science and technology of rapid solidification and processing. Dordrecht: Kluwer; 1995.
[5] Peker A, Johnson WL. Appl Phys Lett 1993;63:2342.
[6] Bruck HA, Christman T, Rosakis AJ, Johnson WL. Scripta Metall Mater 1994;30:429.
[7] Conner RD, Rosakis AJ, Johnson WL, Owen DM. Scripta Mater 1997;37:1373.
[8] Gilbert CJ, Ritchie RO, Johnson WL. Appl Phys Lett 1997;71:476.
[9] Suh DW, Dauskardt RH. J Mater Res 2002;17:1254.
[10] Flores KM, Dauskardt RH. J Mater Res 1999;14:638.
[11] Flores KM, Dauskardt RH. Scripta Mater 1999;41:937.
[12] Brown WF, Aerospace structural metals handbook. West Lafayette, Indiana: Purdue Research Foundation; 1989. p. 47907.
[13] He MY, Hutchinson JW. Eng Fract Mech 2000;65:1.
[14] Newman JC, Raju IS. NASA Tech Memo 1984;85793:1.
[15] Launey ME, Busch R, Kruzic JJ. Acta Mater 2008;56:500.
[16] Zhang ZF, Eckert J, Schultz L. Acta Mater 2003;51:1167.
[17] Lowhaphandu P, Montgomery SL, Lewandowski JJ. Scripta Mater 1999;41:19.
[18] Lewandowski JJ, Lowhaphandu P. Philos Mag A (Phys Conden Matter: Struct, Def Mech Prop) 2002;82:3427.
[19] Liu CT, Heatherly L, Easton DS, Carmichael CA, Schneibel JH, Chen CH, et al. Metall Mater Trans A (Phys Metall Mater Sci) 1998;29A:1811.
[20] Wright WJ, Saha R, Nix WD. Mater Trans 2001;42:642.
[21] Wesseling P, Lowhahphandu P, Lewandowski JJ. Mater Res Soc Symp – Proc 2003;754:275.
[22] Rudnicki JW, Rice JR. J Mech Phys Solid 1975;23:371.
[23] Argon AS, Megusar J, Grant NJ. Scripta Metall 1985;19:591.
[24] Spaepen F. Acta Metall 1977;25:407.
[25] Steif PS, Spaepen F, Hutchinson JW. Acta Metall 1982;30:447.
[26] Flores KM, Dauskardt RH. Acta Mater 2001;49:2527.
[27] Wright WJ. Shear band processes in bulk metallic glasses. Material science and engineering. Stanford, CA: Stanford University Press; 2003. p. 153.
[28] Zhang ZF, Eckert J, Schultz L. Metall Mater Trans A (Phys Metall Mater Sci) 2004;35A:3489.